INTERNATIONAL JOURNAL FOR NUMERICAL METHODS IN ENGINEERING
Int. J. Numer. Meth. Engng 2008; **76**:1159–1184
Published online 19 June 2008 in Wiley InterScience (www.interscience.wiley.com). DOI: 10.1002/nme.2351

Meshfree simulation of failure modes in thin cylinders subjected to combined loads of internal pressure and localized heat

Dong Qian[1,*,†], Thomas Eason[2], Shaofan Li[3] and Wing Kam Liu[4]

[1]*Department of Mechanical Engineering, University of Cincinnati, Cincinnati, OH 45221-0072, U.S.A.*
[2]*Air Force Research Laboratory, Air Vehicles Directory, WPAFB, Dayton, OH 45433-7402, U.S.A.*
[3]*Department of Civil Engineering, University of California, Berkeley, CA 94720-1710, U.S.A.*
[4]*Department of Mechanical Engineering, Northwestern University, Evanston, IL 60208-0311, U.S.A.*

SUMMARY

This paper focuses on the non-linear responses in thin cylindrical structures subjected to combined mechanical and thermal loads. The coupling effects of mechanical deformation and temperature in the material are considered through the development of a thermo-elasto-viscoplastic constitutive model at finite strain. A meshfree Galerkin approach is used to discretize the weak forms of the energy and momentum equations. Due to the different time scales involved in thermal conduction and failure development, an explicit–implicit time integration scheme is developed to link the time scale differences between the two key mechanisms. We apply the developed approach to the analysis of the failure of cylindrical shell subjected to both heat sources and internal pressure. The numerical results show four different failure modes: dynamic fragmentation, single crack with branch, thermally induced cracks and cracks due to the combined effects of pressure and temperature. These results illustrate the important roles of thermal and mechanical loads with different time scales. Copyright © 2008 John Wiley & Sons, Ltd.

Received 19 March 2007; Revised 19 February 2008; Accepted 20 February 2008

KEY WORDS: meshfree method; crack; thermo-mechanical coupling; damage; pressurized cylinder; finite strain

1. INTRODUCTION

There is a continuing interest in the study of material failure in cylindrical shell structures subjected to internal pressure loads. It has been suggested that failure modes in this type of structures are

*Correspondence to: Dong Qian, Department of Mechanical Engineering, University of Cincinnati, Cincinnati, OH 45221-0072, U.S.A.
†E-mail: dong.qian@uc.edu

Contract/grant sponsor: ASEE Air Force Summer Faculty Fellowship Program
Contract/grant sponsor: Air Force Research Lab

triggered by the onset of bifurcation, which further leads to the development of shear bands in ductile materials and, subsequently, fracture. To date, theoretical and numerical studies on this subject have been based on different material models, which include elastic [1, 2], rigid-plastic [3, 4], elasto-plastic [5–10], nonlocal plastic [11] and elasto-viscoplastic models [12–15]. Experimental studies of the failure have been performed in [8] for pressurized cylinders made of either aluminum or copper with different shell wall thicknesses. The failure modes observed for these two materials are very different. Diffusive necking was reported in copper, while surface waves appeared in aluminum tubes.

From the analytical point of view, the initiation of localized failure is a manifestation of material and structural instability. The specific mechanisms can be very different for the cases of quasi-static and dynamic loading. In the former case, the classical bifurcation analysis based on [16–18] applies. It states that localization can be considered as the instability in the macroscopic constitutive description of the inelastic deformation. This condition can be further reduced to the loss of strong ellipticity in the rate form of the governing momentum equation. If a numerical approach such as the finite element method (FEM) is used for the study, one also needs to be cautious about the mesh sensitivity [19] while tracking the post-bifurcation response. In the dynamic case, the governing equation is regularized due to the strain-rate sensitivity of the material. The developments of strain localization and material failure are known to be very sensitive to factors such as initial imperfections and the inertia effects [12, 14, 15, 20]. Compared with the quasi-static case, different failure modes such as multiple necking have been reported [14, 15] due to geometric imperfection.

In most of the numerical simulations discussed above, the focus has been on responses of cylindrical shells under plane strain condition. Under such an assumption, the 3D cylinder model degenerates into a ring model. As noted in [15], this approach is not able to capture the development of material instability modes that are inclined with respect to the tube axis. In addition, the geometric imperfection can only be prescribed in two dimensions. As a result, the effects on the failure mode due to any imperfections in material or geometry along the tube axis are not included. Based on these considerations, one of the main objectives of this paper is to develop a simulation method for pressurized cylinders in three dimensions.

Aside from the dimensional consideration, there also seems to be very little knowledge of the response of cylinders subjected to combined dynamic load and heat. Study of this topic is important for many engineering systems that routinely use cylindrical shell structures and may be exposed to dramatic temperature change. Examples include fuel and gas storage tanks, oil pipes, motor and engine cases and many aerospace components. For instance, the next-generation air vehicles are expected to fly at hypersonic speed range and experience the combinations of extremely high mechanical and thermal loads. Performing experiments to study and verify these applications will be very costly and challenging. As such, we are particularly interested in developing simulation methods to study the roles of the heat-induced softening and strain-rate dependence on the material and structural failure modes. To our knowledge, no systematic study has been presented on this subject in the past.

Two scenarios are possible in the coupled responses between thermal conduction and stress evolution in the materials. If the mechanical (pressure) load is so intensive that the material fails in a relatively short time before the thermal effect takes place, one could adopt the adiabatic approximation and the thermal–mechanical coupling is only reflected in the plastic dissipation. This can greatly simplify the numerical procedure. On the other hand, if the material fails as a result of the combined mechanical load and thermal softening, the effect due to heat conduction

DOI: 10.1002/nme

should also be included in the analysis. In the present formulation, the contributions from both adiabatic heating and conduction are fully taken into account.

In terms of the numerical implementation, the following aspects are considered:

(1) There are large differences in the time scales between heat conduction and mechanical wave propagation. This is reflected in the critical time steps corresponding to the two different mechanisms in the numerical simulation.
(2) The full coupling between thermal and mechanical equations requires careful formulation of the governing equations and material model within the framework of finite deformation.
(3) Simulation of the post-bifurcation requires an efficient numerical algorithm in tracking the initiation and propagation of failure.

In addressing the first aspect, a multi-time-stepping algorithm is developed to bridge the time scale differences between heat conduction and wave propagation. In terms of the material model mentioned in the second aspect, we describe a thermo-elasto-viscoplastic model that accounts for the rate and temperature dependencies, along with two damage criteria that are used for modeling the initiation of material failure.

In terms of numerical approximation, meshfree method has been chosen in this paper because of its unique ability to construct high-order interpolants, which are important for modeling the non-linear responses of shell structures. General reviews on the meshfree and particle methods can be found in [21, 22]. For thin structures such as plates and shells, there are three types of numerical formulations. The first is derived directly from the classical plate or shell theory, the second is based on the so-called continuum-based approach [23] and the third is from the direct application of 3D continuum theory. The first approach is the most difficult as it deals with non-linear plate or shell equations and curvilinear coordinates [24]. Most meshfree methods proposed so far have focused on a continuum-based approach or simply modeled the shell or plate as a standard continuum. A meshfree thin shell formulation based on Kirchhoff–Love theory and element-free Galerkin (EFG) method [25] has been developed by Krysl and Belytschko [26] in the context of small strain, linear elastic framework. Rabczuk *et al.* [27] extended this work with the consideration of finite strain, non-linear elastic material and focused on fracture. In the following work, Rabczuk and Areias [28] have simplified the treatment of cracks in thin shell by using an extrinsic basis. Donning and Liu [29] noted the advantage of meshfree approximations in addressing shear locking in Mindlin type of beams and plates and have developed a meshfree formulation based on the reproducing kernel particle method (RKPM) [30, 31] and a spline-based meshfree approach. This methodology is further extended by Kanok-Nukulchai *et al.* [32] with the use of EFG. It is noted that both EFG and RKPM can be derived based on moving least-squares procedure [21] and therefore the approximations are similar. EFG has been employed by Noguchi *et al.* [33] for shell and membrane structures in which bi-cubic and quartic basis functions are introduced in order to avoid shear and membrane locking. Garcia *et al.* have applied the method of *hp*-cloud [34] in the analysis of the Mindlin plate and demonstrated that shear locking can be controlled with high-order *hp*-cloud approximation. Leitao [35] developed a meshfree method based on radial basis functions (RBF) for modeling a Kirchhoff type of plate. Extension of RBF approach to the Mindlin type of plate was presented in Liew and Chen [36, 37]. The meshless local Petrov–Galerkin was proposed by Atluri *et al.* [38] for solving beam problems and application of this meshfree approach to plates and shells can be found in [39–43]. Wang and Chen showed that the Kirchhoff mode in the Mindlin plate can be reproduced using EFG or RKPM if second-order polynomial basis is used in the moving

DOI: 10.1002/nme

least-squares approximation. By implementing this with a nodal integration and stabilization scheme, they have shown that the formulation is stable and free of shear locking. This approach is further extended to the cases of shells [44] and curved beams [45]. Yagawa and Miyamura [46] developed a free mesh method in which the discrete Kirchhoff theory is combined with the mixed approach. In the case of 3D continuum models, Li *et al.* [47] have presented a formulation based on RKPM and have studied non-linear large deformation of thin shells. Lu *et al.* [48] have combined the RKPM method with an enrichment approach for the simulation of buckling in sheet metal forming.

In this paper, the 3D meshfree continuum approach developed in Li *et al.* [47] is extended to the case of thermo-mechanical coupling. As shown in [47], this approach is relatively simpler in its formulation and implementation than the continuum-based approach. Moreover, the high-order approximations effectively alleviate shear locking, which are typically associated with the use of low-order finite elements. A shortcoming associated with the use of the 3D continuum approach in the explicit computation of thin structure is the short time step, which is limited due to stability requirements. Although several techniques such as mass scaling and artificial damping can be used to alleviate this problem for specific applications, no attempts have been made in this paper as the problem of interest here is transient in nature. Furthermore, the validity of the kinematic assumptions used in plate or shell theory remains unknown for the case of large deformation and non-linear material [24]. Therefore, the direct 3D formulation may lead to better accuracy for the problems that are of interest in this paper.

Based on the simulation results on pressurized cylinder with an initial short narrow opening, we report our observations of different failure modes as different combinations of thermal and pressure loads are applied. In the case of instantaneously applied high pressure and high body heat, the initial opening branches into two cracks that are parallel to the axis of the cylinder on each side. Further loading leads to fragmentation of the cylinder due to the additional cracks initiated from the two sides. In the second loading case, the pressure loading rate is adjusted lower without any heat source. The initial opening is observed to further propagate to both sides without changing the direction. In the third case, it is found that the initial opening will not propagate when very high intensity of body heat is applied instantaneously. Instead, the material fails at the outer edge of the heated zone and is dominated by the extra-high heat input. Finally, multiple cracks due to combined thermal and mechanical loading are observed in the last loading case, which includes both high body heat intensity and pressure load. To our knowledge, the transition among the fragmentation, single crack, thermally induced material failure and combined failure mode in this paper is the first of the kind reported for pressurized cylinders. It is a further extension of the ductile-to-brittle failure transition phenomena previously studied in [49, 50] for an asymmetrically impact-loaded prenotched plate (Kalthoff problem).

The technical details of these implementations as well as the results are outlined in the remainder of the paper, which is organized as follows: In Section 2, the variational forms of the governing equations of momentum and temperature equations are derived. Section 3 describes the shape functions generated from the meshfree method and the discretized equations are presented. The rate- and temperature-dependent constitutive models and the corresponding solution scheme are discussed in Section 4. In Section 5, we further describe a multi-time-stepping algorithm that is designed to accommodate the different time scales associated with the temperature response. Finally, results and discussions are presented in Section 6.

DOI: 10.1002/nme

2. GENERAL VARIATIONAL FORMULATIONS

2.1. Momentum equation

The formulation presented below follows or departs from [50]. We have used the weak form of the conservation of linear momentum within the total Lagrangian framework. This is equivalent to stating that the weak form of the momentum equation is derived in the initial configuration and it is given as [24]

$$\int_{\Omega_0} \mathbf{P}:\boldsymbol{\delta}\mathbf{F}^{\mathrm{T}}\,\mathrm{d}\Omega = \int_{\Omega_0} \rho_0 \mathbf{b_0}\cdot\boldsymbol{\delta}\mathbf{u}\,\mathrm{d}\Omega + \int_{\Gamma_{t0}} \mathbf{T_0}\cdot\boldsymbol{\delta}\mathbf{u}\,\mathrm{d}\Gamma - \int_{\Omega_0} \rho_0 \frac{\partial^2 \mathbf{u}}{\partial t^2}\delta\mathbf{u}\,\mathrm{d}\Omega \tag{1}$$

where $\mathbf{T}_0$ is the prescribed traction on the surface Γ_{t0} and $\mathbf{b}_0$ is the body force on volume Ω_0. Both volume and surface are defined in the reference configuration. The first term on the left of Equation (1) is the first Piola–Kirchhoff stress $\mathbf{P}$, which can be related to the Kirchhoff stress tensor as with $\boldsymbol{\tau}=\mathbf{F}\cdot\mathbf{P}$ with $\mathbf{F}$ as the deformation gradient. Finally, $\mathbf{u}$ is the displacement and $\mathbf{u}=\mathbf{u}_0$ on the essential boundary Γ_{u0} and ρ_0 is the mass density.

2.2. Energy equation

In the reference configuration, the rate form of the energy balance is given as

$$\int_{\Omega_0} \rho_0 \dot{e}\,\mathrm{d}\Omega = \int_{\Omega_0} \boldsymbol{\tau}:\mathbf{D}\,\mathrm{d}\Omega - \int_{\partial\Omega_0} J\hat{\mathbf{N}}\cdot\mathbf{F^{-1}}\cdot\bar{\mathbf{q}}\,\mathrm{d}S + \int_{\Omega_0} \rho_0 s_0\,\mathrm{d}\Omega \tag{2}$$

where e is the internal energy density, $\mathbf{D}$ is the rate of deformation, $J=\det(\mathbf{F}), \hat{\mathbf{N}}$ is defined as the normal of the surface element in the reference configuration, $\bar{\mathbf{q}}$ is the heat flux through the boundary with surface normal $\hat{\mathbf{n}}$ in the current configuration and $\hat{\mathbf{n}}\,\mathrm{d}S = J\hat{\mathbf{N}}\mathbf{F}^{-1}\,\mathrm{d}S_0$. Finally, s_0 is the internal heat source.

The heat flux is proportional to the temperature gradient on the boundary of the body, i.e.

$$\bar{\mathbf{q}} = -\boldsymbol{\kappa}\cdot\frac{\partial T}{\partial \mathbf{x}} = -\boldsymbol{\kappa}\cdot\frac{\partial T}{\partial \mathbf{X}}\cdot\frac{\partial \mathbf{X}}{\partial \mathbf{x}} = -\boldsymbol{\kappa}\cdot\frac{\partial T}{\partial \mathbf{X}}\cdot\mathbf{F}^{-1} = -\boldsymbol{\kappa}\cdot\mathbf{F}^{-\mathrm{T}}\cdot\frac{\partial T}{\partial \mathbf{X}} \tag{3}$$

where $\boldsymbol{\kappa}$ is the heat conductance tensor.

We assume that the thermo-elastic contribution to the internal work is negligible, i.e. $\boldsymbol{\tau}:(\mathbf{D}^e+\mathbf{D}^{\mathrm{T}})=0$ and postulate that the major part of the plastic work will be converted to heat using the factor χ according to [51]. Furthermore, we will use the specific heat at constant pressure c_p to approximate the specific heat at constant stress. The energy balance equation can be further expressed as the following using the Gauss divergence theorem:

$$\int_{\Omega_0} \rho_0 c_p \frac{\partial T}{\partial t}\,\mathrm{d}\Omega = \int_{\Omega_0} (\chi\boldsymbol{\tau}:\mathbf{D}^{\mathrm{p}} + \rho_0 s_0)\,\mathrm{d}\Omega + \int_{\Omega_0} \nabla_X \left(J\mathbf{F^{-1}}\cdot\boldsymbol{\kappa}\cdot\mathbf{F}^{-\mathrm{T}}\cdot\frac{\partial T}{\partial \mathbf{X}}\right)\mathrm{d}\Omega \tag{4}$$

As Equation (4) holds for arbitrary closed volume $\Omega\subset\Omega_0$, it gives the following strong form:

$$\rho_0 c_p \frac{\partial T}{\partial t} = \chi\boldsymbol{\tau}:\mathbf{D}^{\mathrm{p}} + \rho_0 s_0 + \nabla_X (J\mathbf{F}^{-1}\cdot\boldsymbol{\kappa}\cdot\mathbf{F}^{-\mathrm{T}}\nabla_X T) \tag{5}$$

DOI: 10.1002/nme

The weak form of the energy balance equation can be derived based on Equation (5) with the use of integration by parts

$$\int_{\Omega_0} \rho_0 c_p \frac{\partial T}{\partial t} \delta T \, \mathrm{d}\Omega = \int_{\Omega_0} (\chi \boldsymbol{\tau} : \mathbf{D}^{\mathrm{p}} + \rho_0 s_0) \delta T \, \mathrm{d}\Omega + \int_{\partial\Omega_0} J(\mathbf{F}^{-1} \cdot \boldsymbol{\kappa} \cdot \mathbf{F}^{-\mathrm{T}} \nabla_X T) \cdot \hat{\mathbf{N}} \delta T \, \mathrm{d}S - \int_{\Omega_0} J(\mathbf{F}^{-1} \cdot \boldsymbol{\kappa} \cdot \mathbf{F}^{-\mathrm{T}} \nabla_X T) \cdot (\nabla_X \delta T) \, \mathrm{d}\Omega \tag{6}$$

There are two ways to prescribe the heat source. One can either directly apply body heat s_0 or assume that a spatial heat flux $\mathbf{q}_0$ comes towards the object, such that, at part of the object's surface $\Gamma^{\mathrm{temp}} \subset \partial\Omega_0$, one may prescribe

$$\boldsymbol{\kappa} \cdot \mathbf{F}^{-\mathrm{T}} \nabla_X T = -\mathbf{q}_0 \quad \forall \mathbf{X} \in \Gamma^{\mathrm{temp}} \tag{7}$$

Therefore, the weak form (Equation (6)) can be rewritten as

$$\int_{\Omega_0} \rho_0 c_p \frac{\partial T}{\partial t} \delta T \, \mathrm{d}\Omega = \int_{\Omega_0} (\chi \boldsymbol{\tau} : \mathbf{D}^{\mathrm{p}} + \rho_0 s_0) \delta T \, \mathrm{d}\Omega - \int_{\partial\Omega_0} J(\mathbf{F}^{-1} \cdot \mathbf{q_0}) \cdot \hat{\mathbf{N}} \delta T \, \mathrm{d}S - \int_{\Omega_0} J(\mathbf{F}^{-1} \cdot \boldsymbol{\kappa} \cdot \mathbf{F}^{-\mathrm{T}} \nabla_X T) \cdot (\nabla_X \delta T) \, \mathrm{d}\Omega \tag{8}$$

which is the final form of the energy equation.

3. MESHFREE APPROXIMATIONS BASED ON RKPM

To discretize the momentum and temperature equations derived in the last section (Equations (1) and (8)), the meshfree interpolation based on the RKPM developed by Liu *et al.* [30] is introduced. The RKPM was originally developed to improve the robustness of the smoothed particle hydrodynamics (SPH) method. It modifies the kernel function in SPH by introducing a correction function in order to enforce the completeness of the SPH interpolant. Based on RKPM, the meshfree shape function defined at node I is given as

$$N_I(\mathbf{X}) = \mathbf{P}(0)\mathbf{M}^{-1}(\mathbf{X})\mathbf{P}^{\mathrm{T}}\left(\frac{\mathbf{X}-\mathbf{X}_I}{\rho}\right)\Phi_\rho(\mathbf{X}-\mathbf{X}_I)\Delta V_I \tag{9}$$

where $\mathbf{P}$ is the base function. In this paper, the tri-linear polynomial base function is used and $P(\mathbf{X}) = \{1 \;\; X \;\; Y \;\; Z \;\; XY \;\; YZ \;\; XZ \;\; XYZ\}$. In addition, $\mathbf{M}$ is called a moment matrix, Φ_ρ is the window function and ΔV_I is the quadrature weight associated with node I. Readers are referred to [30] for the detailed procedures to construct the shape function based on Equation (9).

Compared with FEM, generating the meshfree shape functions involves an additional procedure to obtain the solution to enforce the reproducing condition [30]. However, as we are adopting a total Lagrangian form [24] of the governing equations, this calculation is implemented only once. In general, meshfree shape functions have larger support size than the FEM shape functions. In computing the nodal internal and external forces in the meshfree method, it is more efficient to construct the loop that occurs over nodes instead of elements due to the nonlocal nature of the approximation. There are also differences in enforcing the essential boundary conditions between

DOI: 10.1002/nme

the two methods as meshfree shape function does not satisfy the Kronecker delta condition. In this paper, we have modified the shape functions at the boundary using a collocation method described in [47, 52] so that the essential boundary conditions can be directly imposed on the nodes. Detailed implementations can be found in these two references.

Based on Equation (9), the displacement and temperature fields are interpolated as

$$\mathbf{u}^{\mathrm{h}}(\mathbf{X},t)=\sum_{I=1}^{NP}N_I(\mathbf{X})\mathbf{d}_I(t) \tag{10}$$

$$\mathbf{T}^{\mathrm{h}}(\mathbf{X},t)=\sum_{I=1}^{NP}N_I(\mathbf{X})\mathbf{T}_I(t) \tag{11}$$

where $\mathbf{d}_I$ and $\mathbf{T}_I$ are the nodal displacement and temperature vectors, respectively. In terms of the discretization based on the meshfree approximation above, three nodes and four Gauss quadrature points are placed through the thickness for the cylinder structure studied in this paper. More details are provided in the results section.

Following the weak form of the governing equations for momentum (Equation (1)) and energy (Equation (6)), the corresponding discrete equations are given as

$$\mathbf{M}\ddot{\mathbf{u}}^{\mathrm{h}}+\mathbf{f}^{\mathrm{int}}=\mathbf{f}^{\mathrm{ext}} \tag{12}$$

$$\mathbf{C}\dot{\mathbf{T}}^{\mathrm{h}}+\mathbf{K}\mathbf{T}^{\mathrm{h}}=\mathbf{h} \tag{13}$$

and $\mathbf{M}$, $\mathbf{C}$ and $\mathbf{K}$ are the mass matrix, heat capacitance and conductance matrix, respectively. Both lumped mass matrix and lumped capacitance matrix are used in the computation, i.e.

$$M_{IJ}=\int_{\Omega_0}\rho_0 N_I N_J\,\mathrm{d}\Omega\approx\begin{cases}\displaystyle\int_{\Omega_0}\rho_0 N_I\,\mathrm{d}\Omega, & I=J\\ 0, & I\neq J\end{cases} \tag{14}$$

and

$$C_{IJ}=\int_{\Omega_0}\rho_0 c_p N_I N_J\,\mathrm{d}\Omega\approx\begin{cases}\displaystyle\int_{\Omega_0}\rho_0 c_p N_I\,\mathrm{d}\Omega, & I=J\\ 0, & I\neq J\end{cases} \tag{15}$$

The other terms in Equations (12) and (13) are given as

$$f_{iI}^{\mathrm{int}}=\int_{\Omega_0}\frac{\partial N_I}{\partial X_j}P_{ji}\,\mathrm{d}\Omega \tag{16}$$

$$f_{iI}^{\mathrm{ext}}=\int_{\Omega_0}N_I\rho_0 b_i\,\mathrm{d}\Omega_0+\int_{\partial\Omega_0}N_I\bar{t}_i^0\,\mathrm{d}S \tag{17}$$

$$K_{IJ}=\int_{\Omega_0}N_{I,j}J\mathbf{F}_{ji}^{-1}\cdot\boldsymbol{\kappa}_{im}\cdot\mathbf{F}_{ml}^{-\mathrm{T}}N_{J,l}\,\mathrm{d}\Omega \tag{18}$$

$$h_I=\int_{\Omega_0}N_I(\chi\tau_{ij}D_{ij}^{\mathrm{p}}+\rho_0 s_0)\,\mathrm{d}\Omega-\int_{\partial\Omega_0}N_I JF_{kl}^{-1}q_{0k}\hat{N}_l\,\mathrm{d}S \tag{19}$$

DOI: 10.1002/nme

4. CONSTITUTIVE RELATIONS AND FAILURE MODEL

In this section, we outline the constitutive relation of the thermo-elasto-viscoplastic solid adopted from [49] in order to evaluate the stress term in Equation (16). The rate form of the constitutive equation reads as follows:

$$\boldsymbol{\tau}^{\nabla} = \mathbf{C} : (\mathbf{D} - \mathbf{D}^{\mathrm{vp}} - \alpha \dot{T} \mathbf{1}) \tag{20}$$

where $\mathbf{C}$ is the elastic stiffness tensor, $\mathbf{1}$ is the second-order identity matrix, α is the thermal expansion coefficient and $\boldsymbol{\tau}^{\nabla}$ is the Jaumann rate of the Kirchhoff stress, which is defined as

$$\boldsymbol{\tau}^{\nabla} \equiv \dot{\boldsymbol{\tau}} - \mathbf{W} \cdot \boldsymbol{\tau} - \boldsymbol{\tau} \cdot \mathbf{W} \tag{21}$$

A von Mises overstress viscoplastic model is considered, i.e.

$$\mathbf{D}^{\mathrm{vp}} = \left(\frac{3\dot{\bar{\varepsilon}}}{2\bar{\sigma}} \right) \mathbf{s}' \tag{22}$$

where

$$\mathbf{s} = \boldsymbol{\tau} - \tfrac{1}{3} \mathrm{tr}(\boldsymbol{\tau}) \mathbf{1} \tag{23}$$

$$\mathbf{s}' = \mathbf{s} - \boldsymbol{\alpha} \tag{24}$$

$$\bar{\sigma}^2 = \tfrac{3}{2} \mathbf{s}' : \mathbf{s}' \tag{25}$$

where $\boldsymbol{\alpha}$ is defined as the back stress. In the present formulation, the evolution of the back stress at finite strain is not considered and $\boldsymbol{\alpha} = 0$.

The thermo-viscoplastic flow is governed by the power law, which is described as

$$\dot{\bar{\varepsilon}} = \dot{\varepsilon}_0 \left[\frac{\bar{\sigma}}{g(\bar{\varepsilon}, T)} \right]^m \tag{26}$$

$$g(\bar{\varepsilon}, T) = \sigma_0 \left(1 + \frac{\bar{\varepsilon}}{\varepsilon_0} \right)^N \left\{ 1 - \delta \left[\exp\left(\frac{T - T_0}{\kappa} \right) - 1 \right] \right\} \tag{27}$$

In Equations (26) and (27), $\dot{\varepsilon}_0$ is a reference strain rate, m is the rate sensitivity parameter, σ_0 is the yield stress, $\varepsilon_0 = \sigma_0 / E$ is the corresponding reference strain and E is Young's modulus, N is the strain hardening exponent, T_0 is a reference temperature and δ, $\boldsymbol{\kappa}$ are thermal softening parameters. Specific values of the model parameters are given in Section 6. The function $g(\bar{\varepsilon}, T)$ is the stress–strain relation measured at quasi-static strain rate of $\dot{\varepsilon}$ at temperature T. The equivalent plastic strain $\bar{\varepsilon}$ is defined as

$$\bar{\varepsilon} = \int_0^t \dot{\bar{\varepsilon}} \, \mathrm{d}t = \int_0^t \sqrt{\tfrac{2}{3} \mathbf{D}^{\mathrm{p}} : \mathbf{D}^{\mathrm{p}}} \, \mathrm{d}t \tag{28}$$

To consider the temperature dependency of the materials, softening in material due to temperature rise is accounted for in the following manner based on [53]:

$$E(T) = E_0 - 1.6 \times 10^6 (T - T_0) - 10^5 (T - T_0)^2 \, \mathrm{Pa} \tag{29}$$

$$\nu(T) = \nu_0 + 5 \times 10^{-5} (T - T_0) \tag{30}$$

DOI: 10.1002/nme

$$\sigma_0(T) = \sigma_0 - 1.5\times 10^3 (T-T_0)^2 \,\mathrm{Pa} \tag{31}$$

$$\alpha(T) = [2.2 + 0.0016(T-T_0)]\times 10^{-5}\,\mathrm{K}^{-1} \tag{32}$$

where E and ν are Young's modulus and the Poisson ratio at temperature T. Furthermore, $E_0 = 200\,\mathrm{GPa}$, $\nu_0 = 0.3$ and $\sigma_0 = 2.0\,\mathrm{GPa}$ are chosen for steel.

The constitutive update scheme for the thermo-elasto-viscoplastic model largely follows the rate tangent modulus approach developed by Peirce *et al.* [54]. The essence of the rate tangent modulus method is to approximate any function of time in the interval $t_{n+\theta} \in [t_n, t_{n+1}]$, $\theta \in [0, 1]$, as

$$f_\theta = (1-\theta) f_n + \theta f_{n+1} \tag{33}$$

Thus, if we choose the predicted velocity field at t_{n+1} as $\mathbf{v}_{n+1}^{\mathrm{trial}} = \mathbf{v}_n + \Delta t \mathbf{a}_n$, then it follows that

$$\mathbf{v}_\theta = (1-\theta)\mathbf{v}_n + \theta \mathbf{v}_{n+1}^{\mathrm{trial}} = \mathbf{v}_n + \theta \Delta t \mathbf{a}_n \tag{34}$$

$$\mathbf{u}_\theta = (1-\theta)\mathbf{u}_n + \theta \mathbf{u}_{n+1} = \mathbf{u}_n + \theta \Delta t \mathbf{v}_n + \theta^2 \Delta t^2 a_n \tag{35}$$

$$\mathbf{L}_\theta = \mathbf{v}_\theta \nabla_x = (\mathbf{v}_\theta \nabla_X) \cdot \mathbf{F}_{n+1}^{-1} \tag{36}$$

$$\mathbf{D}_\theta = \tfrac{1}{2}(\mathbf{L}_\theta + \mathbf{L}_\theta^{\mathrm{T}}) \tag{37}$$

$$\mathbf{W}_\theta = \tfrac{1}{2}(\mathbf{L}_\theta - \mathbf{L}_\theta^{\mathrm{T}}) \tag{38}$$

If we choose $\theta = \frac{1}{2}$, the prediction step, or trial step, corresponds to the central difference scheme mentioned above.

Our goal here is to update the Kirchhoff stress

$$\boldsymbol{\tau}_{n+1} = \boldsymbol{\tau}_n + \dot{\boldsymbol{\tau}}_\theta \Delta t \tag{39}$$

$$\dot{\boldsymbol{\tau}}_\theta \approx \boldsymbol{\tau}_\theta^{\nabla} + \mathbf{W}_\theta \cdot \boldsymbol{\tau}_n + \boldsymbol{\tau}_n \cdot \mathbf{W}_\theta^{\mathrm{T}} \tag{40}$$

To accomplish this, one has to first find $\dot{\bar{\varepsilon}}_\theta$ and then $\boldsymbol{\tau}_\theta^{\nabla}$. Let

$$\dot{\bar{\varepsilon}}_\theta = (1-\theta)\dot{\bar{\varepsilon}}_n + \theta \dot{\bar{\varepsilon}}_{n+1} \tag{41}$$

where $\dot{\bar{\varepsilon}}_{n+1}$ is approximated by a first-order Taylor series expansion in $\bar{\sigma}$, $\bar{\varepsilon}$ and T,

$$\dot{\bar{\varepsilon}}_{n+1} = \dot{\bar{\varepsilon}} + \Delta t_n \left[\left.\frac{\partial \dot{\bar{\varepsilon}}}{\partial \bar{\sigma}}\right|_n \dot{\bar{\sigma}}_\theta + \left.\frac{\partial \dot{\bar{\varepsilon}}}{\partial \bar{\varepsilon}}\right|_n \dot{\bar{\varepsilon}}_\theta + \left.\frac{\partial \dot{\bar{\varepsilon}}}{\partial T}\right|_n \dot{T}_\theta \right] \tag{42}$$

Assume that the temperature update proceeds first, and $\dot{T}_\theta$ comes in handy; based on plastic consistency condition and constitutive relations, one may find that

$$\dot{\bar{\varepsilon}}_\theta \approx \frac{\dot{\bar{\varepsilon}}_n}{1+\xi_\theta} + \frac{1}{H_\theta}\frac{\xi_\theta}{1+\xi_\theta}\left[\mathbf{P}_\theta : \mathbf{D}_\theta + \dot{T}_\theta \left(\frac{\partial \dot{\bar{\varepsilon}}/\partial T}{\partial \dot{\bar{\varepsilon}}/\partial \bar{\sigma}} \right)_n \right] \tag{43}$$

DOI: 10.1002/nme

where

$$\mathbf{P}_\theta = \mathbf{C} : \mathbf{p}_n \tag{44}$$

$$\mathbf{p} = \frac{3}{2}\frac{\mathbf{s}'}{\bar{\sigma}} \tag{45}$$

$$H_\theta \approx -\left.\frac{\partial \dot{\bar{\varepsilon}}/\partial \bar{\varepsilon}}{\partial \dot{\bar{\varepsilon}}/\partial \bar{\sigma}}\right|_n + (\mathbf{p} : \mathbf{L} : \mathbf{p})_n \tag{46}$$

$$\xi_\theta \approx \theta \Delta t \left(\frac{\partial \dot{\bar{\varepsilon}}}{\partial \bar{\sigma}}\right)_\theta H_\theta \tag{47}$$

$$\frac{\partial \dot{\bar{\varepsilon}}}{\partial \bar{\sigma}} = \frac{m \dot{\bar{\varepsilon}}}{\bar{\sigma}} \tag{48}$$

$$\frac{\partial \dot{\bar{\varepsilon}}/\partial T}{\partial \dot{\bar{\varepsilon}}/\partial \bar{\sigma}} = -\left(\frac{\bar{\sigma}}{g(\bar{\varepsilon}, T)}\right)\frac{\partial g}{\partial T} \tag{49}$$

Subsequently following the rate tangent modulus approach [54], the objective rate of the Kirchhoff stress can be given as

$$\boldsymbol{\tau}_\theta^{\nabla} = \mathbf{C}_\theta^{\tan} : \mathbf{D}_\theta - \frac{\dot{\bar{\varepsilon}}_n}{1+\xi_\theta}\mathbf{P}_\theta - \frac{\xi_\theta}{(1+\xi_\theta)H_\theta}\left(\frac{\partial \dot{\bar{\varepsilon}}/\partial T}{\partial \dot{\bar{\varepsilon}}/\partial \bar{\sigma}}\right)_n \dot{T}_\theta \mathbf{P}_\theta - \alpha \dot{T}_\theta \mathbf{C} : \mathbf{1} \tag{50}$$

where

$$\mathbf{C}_\theta^{\tan} = \mathbf{C} - \left(\frac{1}{H}\frac{\xi}{1+\xi}\right)_\theta \mathbf{P}_\theta \otimes \mathbf{P}_\theta \tag{51}$$

Once the objective rate is obtained, the Kirchhoff stress can then be updated according to Equation (39). The corresponding first Piola–Kirchhoff stress in the momentum equation (Equation (1)) is then given as $\mathbf{P} = \mathbf{F}^{-1} \cdot \boldsymbol{\tau}$.

To model the damage failure of the solid, the following two failure conditions are used:

(1) Loss of shear-stress-carrying capacity: This failure condition is explicitly expressed as

$$\bar{\varepsilon}_{\mathrm{cr}} = \varepsilon_1 + (\varepsilon_2 - \varepsilon_1)\frac{\dot{\varepsilon}_r}{(\dot{\varepsilon}_r + \dot{\bar{\varepsilon}})} \tag{52}$$

where ε_1, ε_2 and $\dot{\varepsilon}_r$ are given parameters. After $\dot{\bar{\varepsilon}}$ reaches $\dot{\bar{\varepsilon}}_{\mathrm{cr}}$, the material is assumed to be damaged and therefore it no longer has the shear-stress-carrying capacity. The stress at this stage is modeled by a Newtonian viscous fluid model outlined in [50] and is given as

$$\boldsymbol{\tau} = \frac{\gamma[1 - J + \alpha(T - T_0)]}{J}\frac{E}{(1-\nu)}\mathbf{1} + \mu \mathbf{D} \tag{53}$$

in which γ is the stiffness parameter and μ is the viscosity. The justification to choose such a fluid-type constitutive law is to model the melting process of the inelastic solid at high temperature. More details on the motivation of the model can be found in [50].

DOI: 10.1002/nme

(2) Loss of normal-stress-carrying capacity: To measure the tensile stress failure, the following criterion used in Zhou *et al.* [49] is adopted

$$\sigma_{\max} \geqslant \sigma_{\mathrm{cr}} \tag{54}$$

in which the critical stress is set as $\sigma_{\mathrm{cr}} = 3\sigma_0$. When the maximum principal stress reaches $3\sigma_0$ at a material point, that material point is considered to be completely damaged.

The damage model is implemented at each quadrature point during the constitutive update. Due to the fact that the numerical discretization is meshfree, a particle erosion algorithm is developed to model the initiation and propagation of the crack. The basic idea is as follows: once the complete stress collapse is located at the quadrature point, the particles that are associated with the corresponding integration cell are considered to be completely damaged and thus removed from the simulation. The particle erosion algorithm described here is similar to the element erosion algorithm that has been widely used in FEM. While the numerical implementation of this algorithm is straightforward, it is desirable to have a fine particle density particularly in the vicinity of the failure zone in order to accurately capture the crack propagation. In the current application, the choice of the particle density is limited by the computational hardware that is available for this calculation.

5. THE MULTI-TIME-STEPPING ALGORITHM

In this section, we discuss the time integration algorithm to couple the momentum and temperature equation. The physical process of thermally induced material failure can be divided into two stages based on their time characteristics. The first stage is the temperature rise at extended time durations in which both the heat input and heat conduction are the important contributing factors. The second stage covers a relatively short time period. It starts from the initiation of the material failure and is followed by the crack propagation. Because of the nature of the transient responses in the second stage, one can adopt the adiabatic assumption by neglecting the contribution from the heat conduction. To address the thermo-mechanical coupling in the first stage, we employ the so-called operator-splitting technique developed by Armero and Simo [55]. The basic idea of the operator-splitting approach is to decouple the thermo-mechanical system into two sub-systems: an adiabatic mechanical system and thermal system based on heat conduction. The specific implementations involve two steps: an isentropic step in which the entropy of the system is held fixed and a conduction step at fixed space/time configuration. Following the same philosophy, the contributions to the temperature can be split into two parts: one due to the internal plastic dissipation and instantaneous input and the other due to the conduction. The solution to the temperature equation (Equation (6)) is then decomposed into

$$\text{(1) Adiabatic: } \rho_0 c_p \dot{T}^{\mathrm{a}} = \chi \boldsymbol{\tau} : \mathbf{D}^{\mathrm{p}} + \rho_0 s_0 \tag{55}$$

$$\text{(2) Conduction: } \rho c_p \dot{T}^{\mathrm{c}} = \nabla \cdot (\boldsymbol{\kappa} \cdot \nabla T) \tag{56}$$

in which $\dot{T}^{\mathrm{a}}$ and $\dot{T}^{\mathrm{c}}$ represent the temperature rate due to adiabatic factors such as plastic dissipation and heat source and conduction. Based on the discussion above, the time integration algorithm for the first stage is given as a multi-stepping scheme, which has been developed in the general context of structural dynamics in [56, 57]. If the time step used for solving the discretized temperature equation (Equation (6)) is given as Δt, then the discretized momentum equation (Equation (1)) is solved in m fractional steps with step size $\Delta t/m$. Furthermore, we will use an implicit scheme

DOI: 10.1002/nme

for solving the temperature due to the conduction while using an explicit scheme for updating the mechanical fields and temperature rise due to the internal dissipation. The rationale for the use of this mixed time integration scheme is mainly based on the time characteristic of the temperature responses due to the two different mechanisms and the attributes of the explicit and implicit algorithms. Implicit time algorithms are mostly unconditionally stable, which makes the use of a large time step possible. However, the computational cost to achieve convergence is high and iteration becomes expensive for large-scale problems. On the other hand, explicit algorithms are much less expensive per time step but require small time step size due to the stability requirement. The conduction and dissipation mechanisms provided in this application automatically provide a decomposition of the slow and fast time scale responses. Using explicit time integration for solving the temperature due to the conduction will not be appropriate as the temperature response due to the conduction takes place on a slow time scale. On the other hand, using a implicit algorithm for dissipation-induced temperature rise is likely to have problem with convergence as the time response is of small time scale and oscillatory in nature. In the following, we briefly summarize the solution scheme. An index v is used for the subincremental steps within step n.

(1) Within each subincremental step v, the mechanical fields defined at the nodes are updated through a central difference scheme given as follows:

$$\mathbf{f}_v = \mathbf{f}_v^{\text{ext}} - \mathbf{f}_v^{\text{int}} \tag{57}$$

$$\mathbf{a}_v = \mathbf{M}^{-1}\mathbf{f}_v \tag{58}$$

$$\mathbf{v}_{v+1/2} = \mathbf{v}_{v-1/2} + \frac{\Delta t}{m}\mathbf{a}_v \tag{59}$$

$$\mathbf{u}_{v+1} = \mathbf{u}_v + \frac{\Delta t}{m}\mathbf{v}_{v+1/2} \tag{60}$$

The plastic dissipation can be obtained while solving $\mathbf{f}_v^{\text{int}}$ based on the constitutive law. Correspondingly, the adiabatic contribution to the temperature at each node is computed as

$$\dot{\mathbf{T}}_v^{\text{a}} = \mathbf{C}^{-1}\mathbf{h}_v \tag{61}$$

$$\mathbf{T}_v^{\text{a}} = \mathbf{T}_{v-1}^{\text{a}} + \dot{\mathbf{T}}_v^{\text{a}}\frac{\Delta t}{m} \tag{62}$$

(2) At each time step n, the contribution from the heat conduction is computed as

$$\dot{\mathbf{T}}_n^{\text{c}} = \mathbf{C}^{-1}\mathbf{K}\mathbf{T}_n^{\text{c}} \tag{63}$$

We will employ the α-method for updating the temperature at step $n+1$. The basic idea is to develop a predictor

$$\tilde{\mathbf{T}}_{n+1}^{\text{c}} = \mathbf{T}_n^{\text{c}} + \alpha\Delta t\dot{\mathbf{T}}_n^{\text{c}} \tag{64}$$

and solve

$$\mathbf{C}\frac{\mathbf{T}_{n+1}^{\text{c}} - \tilde{\mathbf{T}}_{n+1}^{\text{c}}}{(1-\alpha)\Delta t} + \mathbf{K}\mathbf{T}_{n+1}^{\text{c}} = 0 \tag{65}$$

The final temperature at step $n+1$ is then updated through

$$\mathbf{T}_{n+1} = \mathbf{T}_{n+1}^{\text{a}} + \mathbf{T}_{n+1}^{\text{c}} \tag{66}$$

DOI: 10.1002/nme

For the example problem to be outlined later, the parameter α is chosen to be $\frac{1}{2}$. The fractional step number $m = 100$. Once the failure is initiated, the contribution from the conduction is regarded as negligible and therefore the implicit algorithm outlined above is no longer being implemented.

6. RESULTS AND DISCUSSIONS

The configuration of the problem is shown in Figure 1. The cylinder considered has an axial length of 1.2 m. The circular cross-section has a mean radius of 22.575 cm and thickness of 0.15 cm. With the exception of a region in which an initial short narrow opening is prescribed in order to initiate the crack, the whole structure is discretized with uniformly distributed 121 nodes in the axial direction, 240 nodes in the circumferential direction and 3 nodes in the radial direction. This leads to a total of 87 063 computational particles. The prescribed opening is aligned with the axis of cylinder and dimension is given as $0.2\,\text{m} \times 0.012\,\text{m} \times 0.0015\,\text{m}$ (Figure 1). Due to this imperfection, meshfree shape functions for the particles in the close vicinity of the opening are modified using the visibility criterion developed by Krysl and Belytschko [58]. To integrate the momentum and temperature equations, a total of 460 160 Gauss points are used for quadrature evaluation. The constitutive equations are then solved at each Gauss point. The numerical discretization based on the meshfree method is shown in Figure 2. A heat source is applied in the local region marked in Figure 2. Different types of body heat are used to examine the effect of thermal softening. The heat zone has a circular shape with a radius of 0.15 m if the cylinder is unfolded onto a plane. All the computational particles are assigned with an initial temperature of 293 K before the body heat

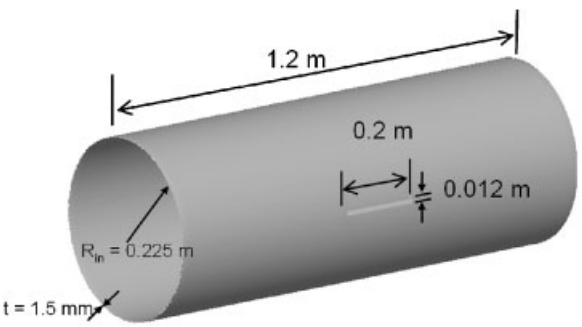

Figure 1. Dimension of the pressurized cylinder problem.

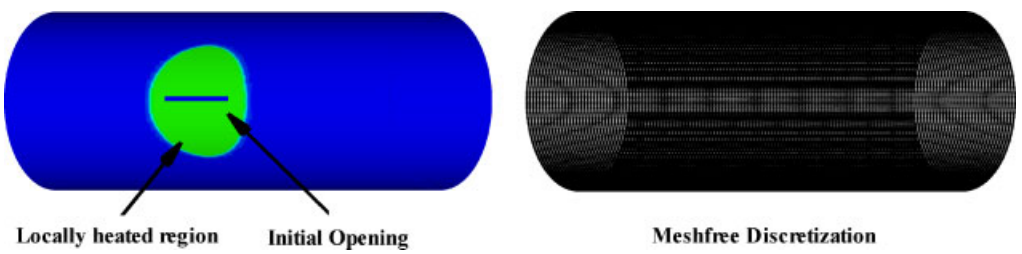

Figure 2. The prescribed temperature zone and meshfree discretization for the pressurized cylinder problem.

DOI: 10.1002/nme

is applied. To mimic the effect of a closed cylinder, tractions of magnitude t are applied on both ends of the cylinder. It is related to the internal pressure p through $\sigma = pd_i/4t$ with d_i being the inner diameter and t being the thickness.

The thermo-viscoplastic model described previously is used to account for the rate and temperature dependence of the material. A time step of 2×10^{-8} s is chosen such that the stability criteria associated with the time integration and constitutive updates are satisfied. The material parameters for the constitutive model represent steel [50] and are listed in Table I.

Four loading cases are considered in this paper. The histories of the mechanical and thermal loads are shown in Figure 3. The main differences are in the rate and intensity of the pressure load and the intensity of body heat. In case I, an internal pressure of 22.8 MPa and localized body heat of $4\,\mathrm{TW/m^3}$ are applied instantaneously. In cases II and III, the initial internal pressure is 0 and increased at a constant rate of $0.0152\,\mathrm{MPa/\mu s}$. In both cases II and III, the computation terminates before $1000\,\mu$s. Therefore, the final pressure in both cases is less than 15.2 MPa. In terms of the thermal load, no heat is applied in case II, while a body heat of $10\,\mathrm{TW/m^3}$ is applied within the same area in case III. In case IV, the pressure load remains the same as in cases II and III, while a body heat rate of $10\,\mathrm{TW/m^3}$ per $1000\,\mu$s is applied. Note that the values on the axis are for illustration only and not drawn proportionally in Figure 3. Based on the individual loading cases, the computation is continued until the failure leads to a negative Jacobian in the

Table I. Material model parameters for the proposed simulation.

Parameter	Value	Definition
$\dot{\varepsilon}_0$	$0.001/\mathrm{s}$	Reference strain rate
m	70	Rate sensitivity parameter
n	0.01	Strain hardening parameter
T_0	293 K	Reference temperature
δ	0.5	Thermal softening parameter
κ	1000 K	Thermal softening parameter
ρ	$7830\,\mathrm{kg/m^3}$	Mass density
c_p	$448\,\mathrm{J/(kg\,K)}$	Specific heat
χ	0.9	The fraction of plastic work converted to heat
ε_1	$4\varepsilon_0$	Damage parameter
ε_2	0.3	Damage parameter
$\dot{\varepsilon}_r$	$4 \times 10^4/\mathrm{s}$	Damage parameter

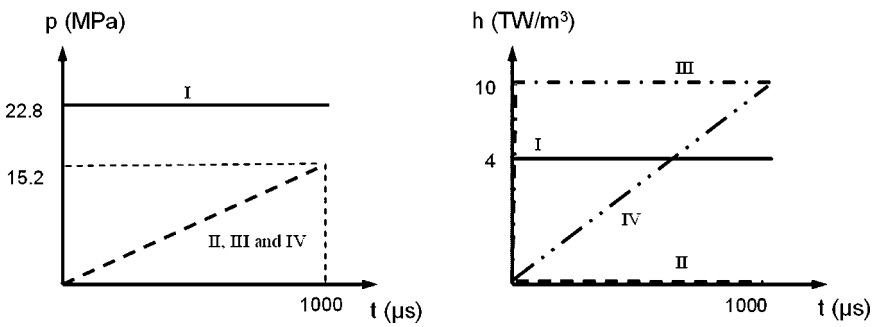

Figure 3. The pressure and heat loading history for the cylinder problem.

DOI: 10.1002/nme

numerical evaluation of the volume. As a brief summary, the major features of the loading are as follows:

(1) *Case I*: Instantaneous high pressure and moderate body heat.
(2) *Case II*: Relative slow pressure loading rate, no heat.
(3) *Case III*: Relative slow pressure loading rate, instantaneous high heat.
(4) *Case IV*: Relatively slow pressure loading rate and body heat rate.

Results generated from these cases are provided below.

6.1. Case I: instantaneous pressure and body heat

In Figure 4 we plotted the time history of the effective stress at 20, 80, 160, 240, 260 and 277.2 μs, along with the deformation in the cylinder. The back half of the cylinder is blanked in order to show the evolution of the material failure. In the initial stage of the crack, one can see the stress wave coming from both ends due to the instantly imposed traction t. In the second frame ($t=80\,\mu$s), the initial sharp crack is blunted and propagates in a radial fashion, centering the original tip. At $\sim 240\,\mu$s, multiple cracks are initiated at the two ends of the cylinder in addition to the further opening of the center crack. Most of the failure developments take place in the last 30 μs. At the initial stage, the prescribed narrow opening branches into two cracks that are parallel to the axis of the cylinder on both sides. Following this, new cracks initiate from the two ends and they further propagate towards the inner portion of the cylinder along the longitudinal direction. One interesting observation in the failure at the final step ($t=277.2\,\mu$s) is that the side and center cracks do not overlap. Because the side portion of the cylinder is now broken into multiple pieces, this case is referred to as a case of fragmentation. Such a failure pattern is observed to be driven by the stress wave. The simulation results are similar to the case of surface wave pattern as reported in [8]. If a cutting plane is made perpendicular to the cylinder axis at the side portion, we shall see fragmented rings under intensive pressure load, which is in the same spirit as the simulation results reported in [14, 15].

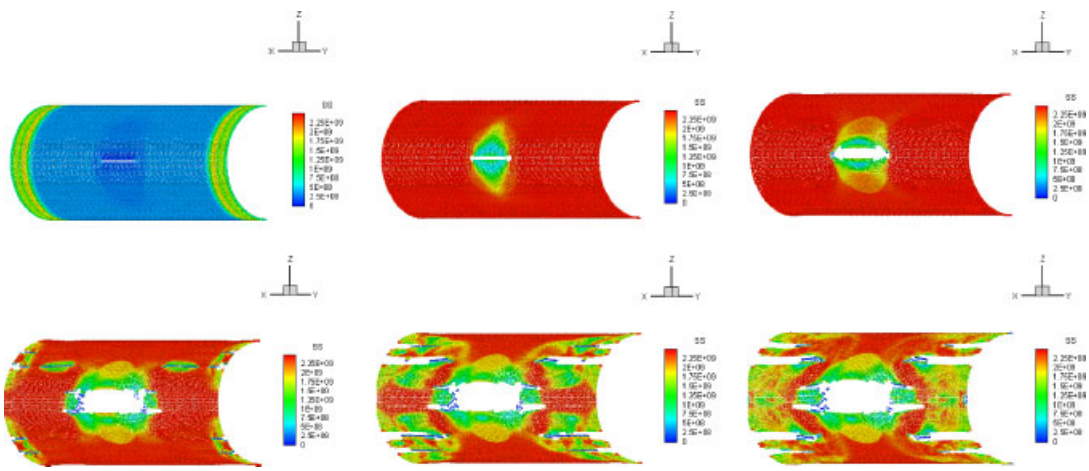

Figure 4. From top left to bottom right: the effective stress history at 20, 80, 160, 240, 260 and 277.2 μs.

DOI: 10.1002/nme

The corresponding temperature (in Kelvin unit) history is shown in Figure 5 for the same time steps. Based on the shape of the heated zone, the temperature rise seems to be dominated by the body heat and plastic dissipation. This can be justified by turning off the solution to the conduction equation and comparing the results (more discussions are provided later). Therefore, the adiabatic assumption is a valid approximation in the present case. Zones of higher temperatures are located in the last three frames and they are all parallel to the cylinder axis. We further note some hot spots at the intersection of the crack and heated zone. The observed maximum temperature in this case is 777 K.

We further examine the results generated above by trying two more different particle discretization schemes in addition to the one already being used. The particle distributions for the three schemes are listed in Table II and are referred to as fine, medium and coarse. The numbers of particles for the medium and coarse discretization cases are 43 560 and 21 960, respectively. The history of the radial expansion obtained from these three different particle discretizations are shown in Figure 6. Here the radial expansion is defined as the maximum radial displacement measured from the simulation data. As can be seen, all the results follow the same trajectory. The main difference is in the time of termination, which is related to the erosion algorithm used here and the ability of the meshfree approximation to reproduce large deformation before producing a negative Jacobian. The fine particle distribution provides a more accurate representation of the material failure.

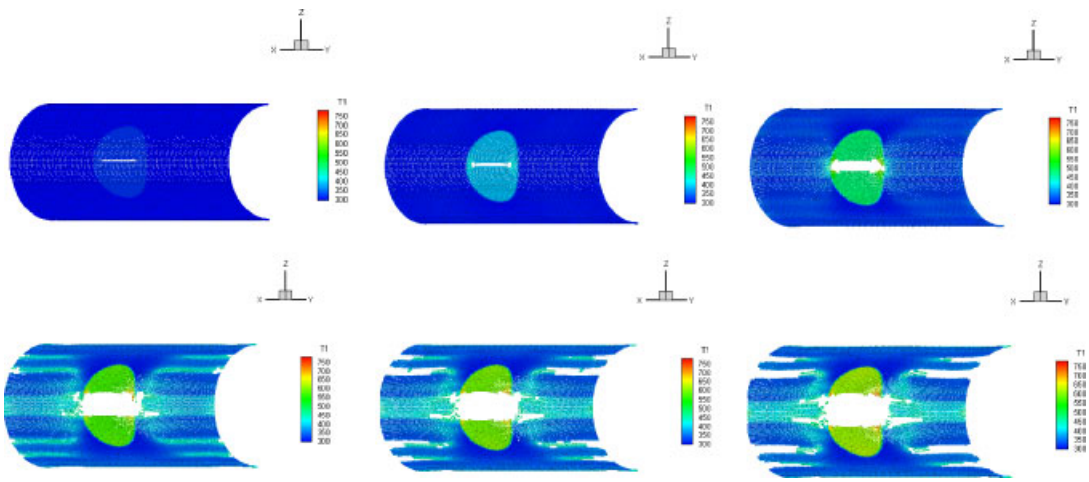

Figure 5. From top left to bottom right: the temperature history at 20, 80, 160, 240, 260 and 277.2 μs.

Table II. Particle discretization schemes used for verifying the results.

	Coarse	Medium	Fine
Axial direction	61	121	121
Circumferential direction	120	120	240
Radial direction	3	3	3

DOI: 10.1002/nme

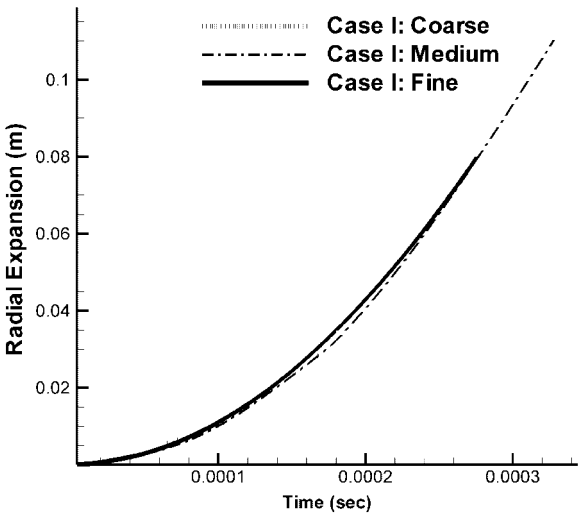

Figure 6. Radial expansion history obtained for load case I with three different particle discretization schemes.

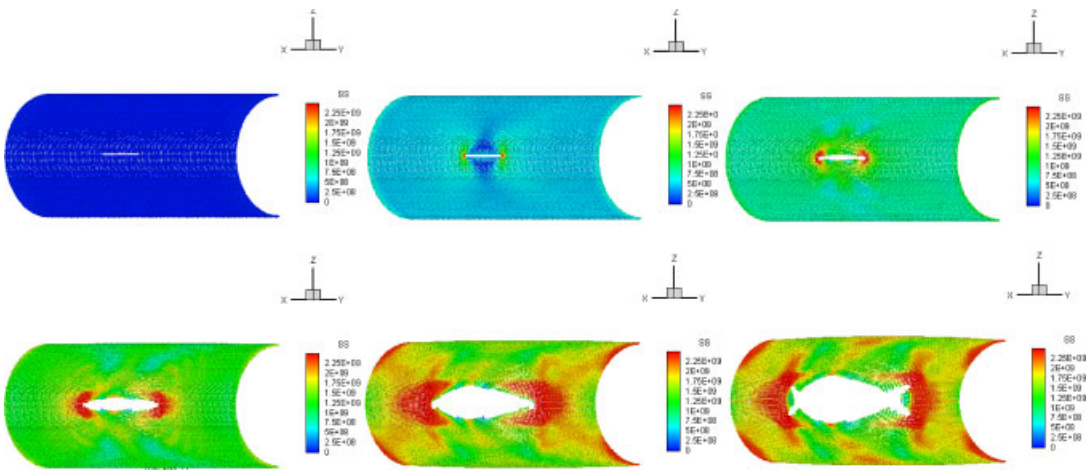

Figure 7. Case II: effective stress history at 20, 200, 400, 600, 800 and 889.08 μs.

6.2. *Case II: constant pressure loading rate without external heat*

According to the loading history for case II shown in Figure 3, the rate at which the pressure is applied is 15.2 MPa per 1000 μs. Therefore, the load is applied at slower rate compared with the previous case. In addition, no external heat is applied and the temperature rise is mainly due to plastic dissipation. The effective stress history and deformation histories are shown in Figure 7. The frames correspond to 20, 200, 400, 600, 800 and 889.08 μs, respectively. The last frame shows the last step before the computation is terminated and the corresponding pressure at failure

DOI: 10.1002/nme

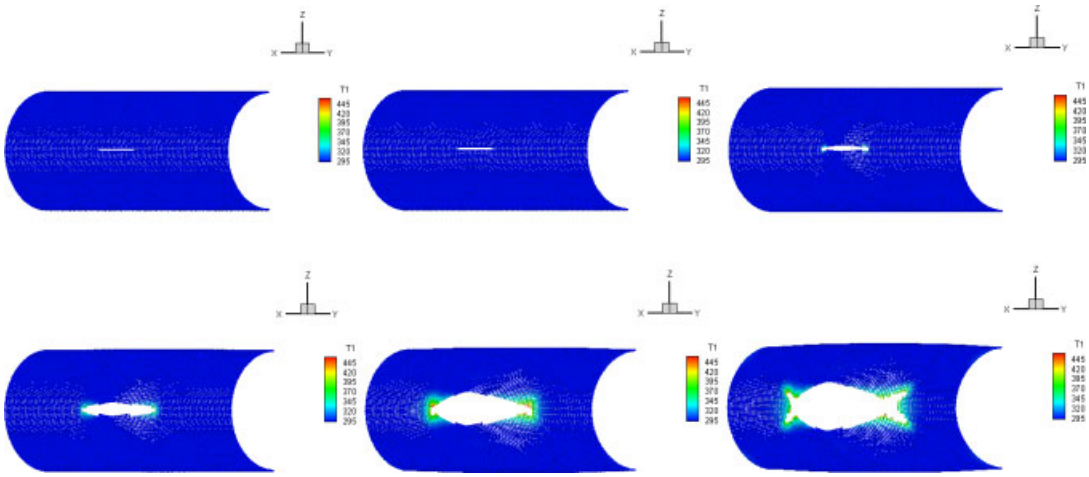

Figure 8. Case II: temperature history at 20, 200, 400, 600, 800 and 889.08 μs.

is 13.514 MPa. From the snapshots, it can be seen that the single crack initiated from the prescribed tip further propagates in the direction parallel to the tube axis. Two stress concentration zones can be located in the close vicinity of the crack tip and they propagate with the crack. The size of the zone increases as the crack further opens up and the initial crack tips become blunted. In the last frame, the single crack develops into a branched pattern on both sides. No shear band formation is observed during the simulation and failure modes are dominated by the fracture.

By further examining the temperature profile in Figure 8, it is observed that most of the region shows no signs of significant temperature increase except for those at the crack tip. A relative high-temperature spot comes in only during the last stage of the load. The highest value of temperature is 460 K.

6.3. Case III: lower pressure loading rate with instantaneous high body heat

In case III, the localized body heat is instantaneously increased to $10\,\mathrm{TW/m^3}$, whereas the mechanical loads are maintained the same as in case II. The effective stress history is plotted along with the deformation in Figure 9 at time instances 20, 100, 200, 300, 360 and 379.22 μs and the numerical computation stops at $t = 379.22\,\mu\mathrm{s}$. In this case, it can be seen that the initial crack tip has shown little sign of further opening or propagating. At the perimeter of the heated zone, a high-stress concentration area is shown starting from the third time frame ($t = 200\,\mu\mathrm{s}$). As the thermal and mechanical loads further progress, multiple cracks are initiated in the same area. Compared with case II, the failure pattern is different and such a pattern is clearly the results of dramatically increased thermal load and the associated loading rate. As the perimeter of the heated zone is almost completely 'eroded' due to the intensive heat, there is a sharp decrease in the effective stress within the same zone, indicating the separation of the heat zone from the rest of the cylinder and consequently loss of load-carrying capacity. Figure 10 gives the temperature history corresponding to those in Figure 9. We noted that the temperature increases faster and the final temperature is much higher than the previous two cases.

DOI: 10.1002/nme

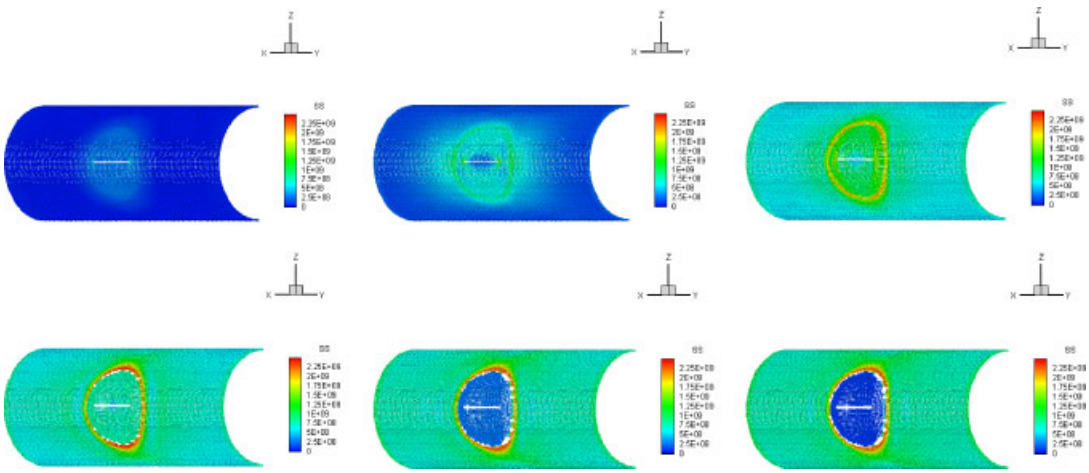

Figure 9. Case III: effective stress history at 20, 100, 200, 300, 360 and 379.22 μs.

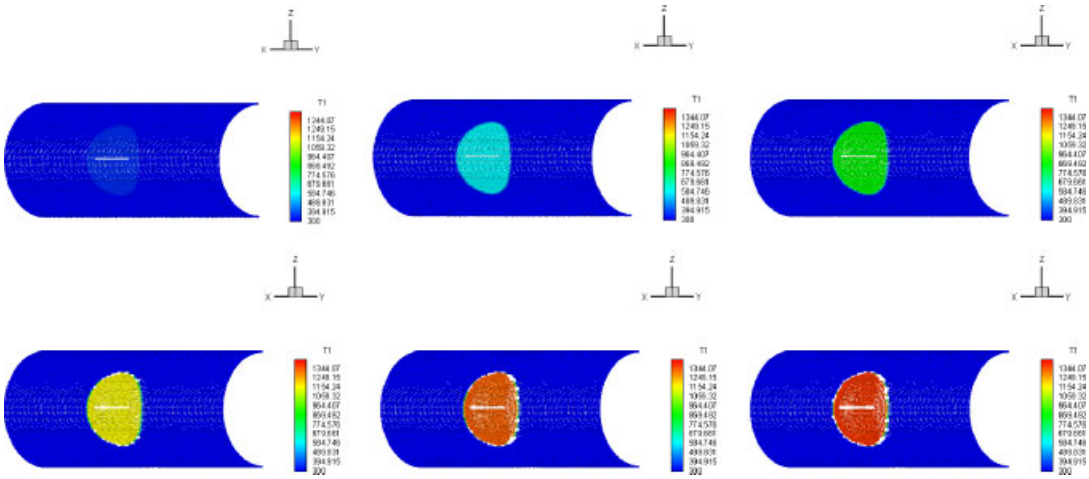

Figure 10. Case III: temperature history at 20, 100, 200, 300, 360 and 379.22 μs.

6.4. Case IV: lower pressure loading rate and body heat rate

Compared with case III, the only difference in the loading in case IV is that a moderate body heat rate is imposed. Comparing Figure 9 with Figure 11, we find that the failure patterns are completely different. The computation terminates at 844 μs, which is longer than the 379.22 μs in the previous case. Two types of failure patterns co-exist by examining Figure 11. The first type is similar to case III and is characterized by the curved cracks at the perimeter of the heated zone. The second type is similar to case II and is the direct result of the initial crack further opening and propagation. In the initial stage of the load (before 400 μs), the mechanical load seems to be dominating the process. We can see clearly a stress concentration at the tip of the initial crack. No initiation of body heat-induced crack is observed. However, as the mechanical and thermal

DOI: 10.1002/nme

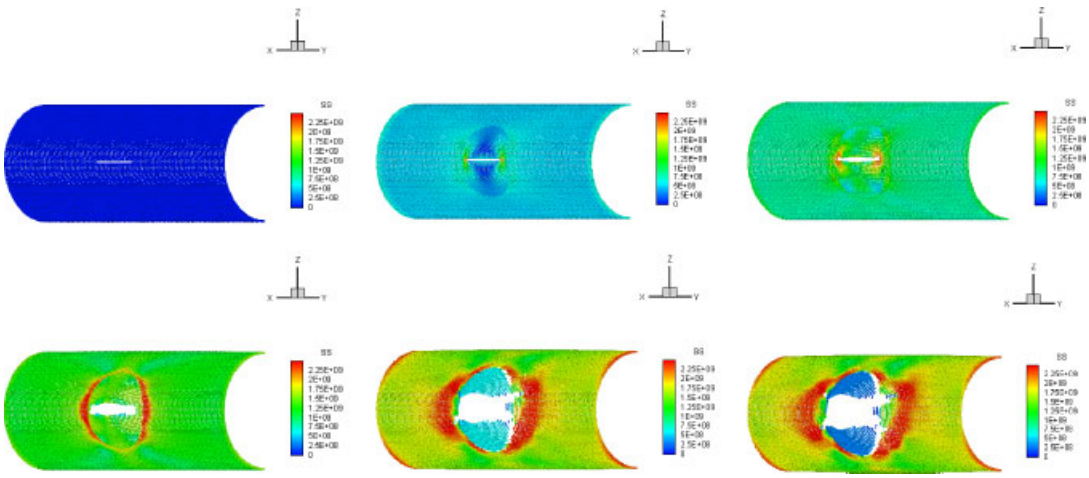

Figure 11. Case IV: effective stress history at 4, 200, 400, 600, 800 and 844 μs.

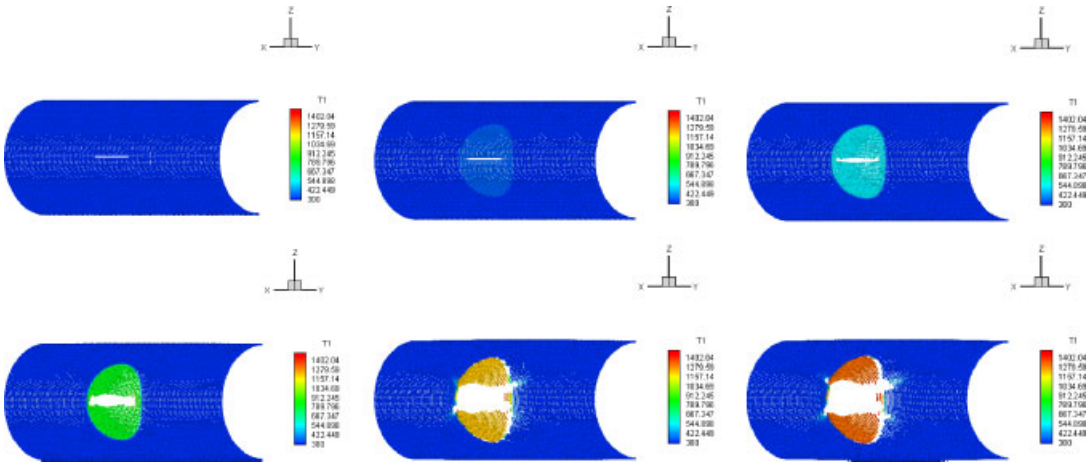

Figure 12. Case IV: temperature history at 4, 200, 400, 600, 800 and 844 μs.

load further progress, we see a stress concentration near the boundary of the heated zone. This is an indication that the thermal effect due to applied body heat has started to have an influence. Based on the deformation shown, the radial expansion in this case is significant and can be clearly observed. Figure 12 shows the temperature history for the same time instances as in Figure 11. Based on the legend, we see that the highest temperature is 1444 K and is shown in the final stage of the loading. This temperature is comparable with that of case III.

6.5. Discussion

With the development of the 3D thermo-mechanical coupling approach, different failure modes have been observed in the simulation of thin pressurized cylinders. These modes are due to the

DOI: 10.1002/nme

initial imperfection and sensitive to the rates and magnitudes of the applied mechanical and thermal loads. There is a competing mechanism between mechanically and thermally induced failure. The rate of the pressure load has significant effects on the failure pattern, which are illustrated in cases I and II. Fragmentations are observed if instantly high pressure is applied, whereas a single crack with branches is found in the case of pressure being applied at a slower rate. The initiation of the crack starts at 57.96 μs in case I and at 333.38 μs in case II. Based on these results, we postulate that the failure is driven by strain rate if the mechanical loads dominate. This is consistent with the strain-rate-dependent failure criteria we have used for accounting the loss of shear-stress-carrying capacity. The thermal-induced failure, on the other hand, is influenced by both the rate and the magnitude of the body heat imposed. Failure occurs at places where one observes large temperature gradient.

To quantify the evolution of the material failure, we introduce a damage index, defined as the ratio of the computational particles being deleted with respect to the total number of particles. The relationship between the damage index and time is plotted in Figure 13. We observe large differences between case I and the other cases. The damage grows at a moderate rate before 0.0002 s and then suddenly accelerates. The slope of the curve shows that the damage continues to accelerate till the last computational step. The final damage index in this case is 0.042 and the process can be characterized as an 'unsteady' crack. In contrast, the damage evolutions in both cases II and IV are 'steady' and are similar to each other before 0.0005 s. Between 0.0005 and 0.0007 s, the damage in the case of pure pressure load develops faster than the case of combined pressure/thermal loads. The effect of the body heat shows up for time after 0.0007 s in case IV. The final damage indices for both cases II and IV are close and remain under 0.01. The damage history for case III corresponds to the intensive heat load and it can be seen that the final damage index is the lowest of all cases. In addition, the time at the last computational step is relatively short. The radial expansion history of the cylinder is shown in Figure 14. The trends in the time history here are very similar to the ones observed in the comparison of the damage. The 3D effects are

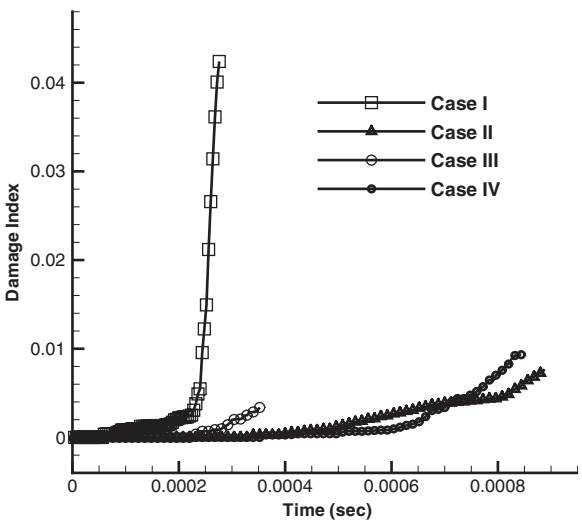

Figure 13. The evolution of the damage index for the four loading cases.

DOI: 10.1002/nme

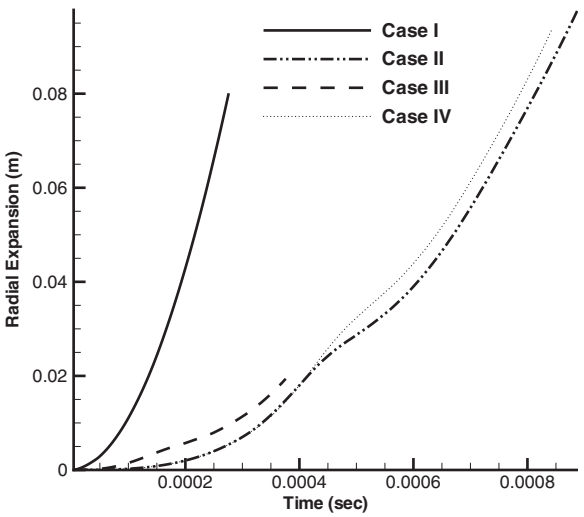

Figure 14. The radial expansion for the four loading cases.

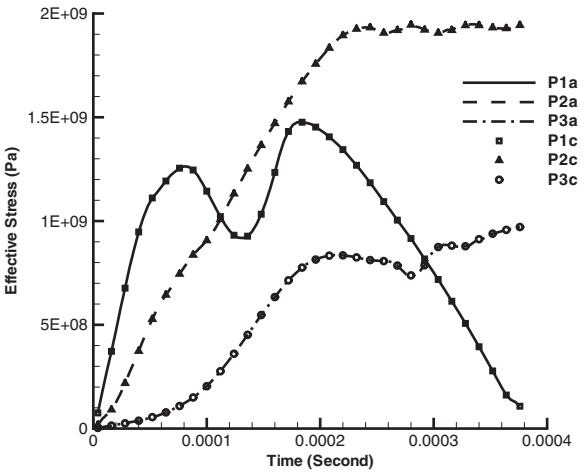

Figure 15. Comparison of effective stress histories for three points.

clearly illustrated through the propagation patterns of the crack in all of the loading cases. In all the examples, the geometric imperfection is prescribed mainly in the form of initial opening; no non-uniform thickness has been considered as in the cited work by other groups.

To verify the effect of thermal conduction, we repeat the computation of case III but turn off the computation associated with the conduction equation. In both cases, we observe that the crack initiates at the same time ($t = 223.06\,\mu s$). We further pick three points along the center of the initial opening. The first point is located at the tip. The second is at the outer boundary of the heated zone and the third is on the left end of the cylinder. The coordinates of the three points are given as $P1$: $(0.2265, -0.1, 0)$, $P2$: $(0.2265, -0.15, 0)$ and $P3$: $(0.2265, -0.6, 0)$. The effective stress

DOI: 10.1002/nme

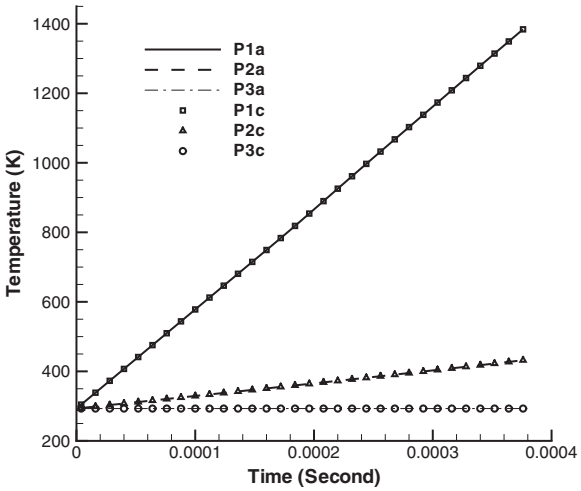

Figure 16. Comparison of temperature histories for three points.

history for the three points are shown in Figure 15. The legend $P1$a stands for the results from the adiabatic case and the other follows a similar definition. It can be seen that the adiabatic and conduction cases fit each other. Some minor differences are observed in the computed data for the effective stresses, but the difference is too small to be visible from the graph. The comparison of the temperature for the same points is shown in Figure 16. A similar conclusion on the effect of conduction can be drawn.

7. CONCLUSIONS

With the developments of a non-linear meshfree method and a thermo-visco-plastic material model, we studied the failure modes in a pressurized cylinder subjected to a localized heat source. Different failure modes are observed when different types of thermal and mechanical loads are applied. Based on the observations, we identified four types of failure modes: (1) dynamic fragmentation due to instantaneously applied pressure; (2) a single crack propagation and branch due to pressure of constant rate; (3) cracks due to intensive body heat; and (4) cracks due to combined thermal and mechanical loads. For all of the cases studied here, the initial imperfection is prescribed in the form of a short narrow opening. The 3D effects of the initial imperfection and the failure evolutions are clearly illustrated through the four loading cases shown.

Although the parametric study of the loading cases here is limited, it is clear that fast pressure loading rate with large magnitude leads to fragmentation, which is of a brittle nature and can be characterized as an 'unstable crack' as defined in [14]. On the other hand, formation of steady cracks is the result of loads being applied at relatively slower load rate. The material failure induced by thermal softening due to intensive heat is an important mode that should be considered in the case of combined thermo-mechanical loading. The final failure mode in such a case depends strongly on both the magnitude and the rate of the mechanical and thermal loads. For the dimensions considered in this case, a rough estimate on the critical mechanical and thermal loads can be

DOI: 10.1002/nme

derived based on the numerical examples. It is important to note that the present study so far has only focused on thin cylinders and no geometric effect has been included. The developed numerical tools can be further extended to explore the effects of these important factors on the failure. Finally, other numerical techniques such as these using cohesive interfaces or enrichment based on discontinuities can be introduced for effectively modeling the evolution of the failure.

ACKNOWLEDGEMENTS

The work of D. Q. is partially supported by the ASEE Air Force Summer Faculty Fellowship program and Air Force Research Lab.

REFERENCES

1. Haughton DM, Ogden RW. Bifurcation of inflated circular cylinders of elastic material under axial loading. II. Exact theory for thin-walled tubes. *Journal of the Mechanics and Physics of Solids* 1979; **27**:489–512.
2. Haughton DM, Ogden RW. Bifurcation of inflated circular cylinders of elastic material under axial loading. I. Membrane theory for thin-walled structures. *Journal of the Mechanics and Physics of Solids* 1979; **27**:179–212.
3. Strifors H, Storakers B. Uniqueness and stability at finite deformation of rigid plastic thick-walled cylinders under hydrostatic pressure. In *Foundations of Plasticity*, Sawczuk S (ed.). Nordhoff: Leiden, 1973; 327.
4. Storakers B. Bifurcation and instability models in thick-walled rigid-plastic cylinder under pressure. *Journal of the Mechanics and Physics of Solids* 1971; **19**:339–351.
5. Chu CC. Bifurcation of elastic–plastic circular cylindrical shells under internal pressure. *Journal of Applied Mechanics—Transactions of the ASME* 1979; **46**:889–894.
6. Tomita Y, Shindo A, Nagai M. Axisymmetric deformation of circular elastic plastic tubes under axial tension and internal-pressure. *International Journal of Mechanical Sciences* 1984; **26**(6–8):437–444.
7. Papanastasiou P, Durban D. Bifurcation of elastoplastic pressure-sensitive hollow cylinders. *Journal of Applied Mechanics—Transactions of the ASME* 1999; **66**(1):117–123.
8. Larsson M, Needleman A, Tvergaard V, Stroakers B. Instability and failure of internally pressurized ductile metal cylinders. *Journal of the Mechanics and Physics of Solids* 1982; **30**(3):121–154.
9. Tvergaard V. Bifurcation in elastic–plastic tubes under internal-pressure. *European Journal of Mechanics A—Solids* 1990; **9**(1):21–35.
10. Mercier S, Molinari A. Analysis of multiple necking in rings under rapid radial expansion. *International Journal of Impact Engineering* 2004; **30**(4):403–419.
11. Mikkelsen LP, Tvergaard V. A nonlocal two-dimensional analysis of instabilities in tubes under internal pressure. *Journal of the Mechanics and Physics of Solids* 1999; **47**(4):953–969.
12. Tugcu P. Inertial effects in ductile failure of cylindrical tubes under internal pressure. *International Journal of Impact Engineering* 1996; **18**(5):539–563.
13. Tugcu P. Failure of internally pressurized cylindrical-tubes for strain rate-dependent materials. *International Journal of Engineering Science* 1995; **33**(11):1581–1594.
14. Sorensen NJ, Freund LB. Unstable neck formation in a ductile ring subjected to impulsive radial loading. *International Journal of Solids and Structures* 2000; **37**(16):2265–2283.
15. Han JB, Tvergaard V. Effect of inertia on the necking behavior of ring specimens under rapid radial expansion. *European Journal of Mechanics A—Solids* 1995; **14**(2):287–307.
16. Hill R. Acceleration waves in solids. *Journal of the Mechanics and Physics of Solids* 1962; **10**:1–16.
17. Rice JR. The localization of plastic deformation. *Proceedings of the 14th IUTAM Congress*. North-Holland: Amsterdam, 1976.
18. Rudnicki JW, Rice JR. Conditions for localization of deformation in pressure-sensitive dilatant materials. *Journal of the Mechanics and Physics of Solids* 1975; **23**:371–394.
19. Needleman A. Material rate dependence and mesh sensitivity in localization problems. *Computer Methods in Applied Mechanics and Engineering* 1988; **67**(1):69–85.
20. Belytschko T, Moran B, Kulkarni M. On the crucial role of imperfections in quasi-static viscoplastic solutions. *Journal of Applied Mechanics—Transactions of the ASME* 1991; **58**(3):658–665.

DOI: 10.1002/nme

21. Belytschko T, Krongauz Y, Organ D, Fleming M, Krysl P. Meshless methods: an overview and recent developments. *Computer Methods in Applied Mechanics and Engineering* 1996; **139**(1–4):3–47.
22. Li SF, Liu WK. *Meshfree Particle Methods*. Springer: Berlin, 2004.
23. Stanley G. Continuum-based shell elements. *Ph.D. Thesis*, Stanford University, 1985.
24. Belytschko T, Liu WK, Moran B. *Nonlinear Finite Elements for Continua and Structures*. Wiley: New York, 2000.
25. Belytschko T, Lu YY, Gu L. Element-free Galerkin methods. *International Journal for Numerical Methods in Engineering* 1994; **37**(2):229–256.
26. Krysl P, Belytschko T. Analysis of thin shells by the element-free Galerkin method. *International Journal of Solids and Structures* 1996; **33**(20–22):3057–3078.
27. Rabczuk T, Areias PMA, Belytschko T. A meshfree thin shell method for non-linear dynamic fracture. *International Journal for Numerical Methods in Engineering* 2007; **72**(5):524–548.
28. Rabczuk T, Areias P. A meshfree thin shell for arbitrary evolving cracks based on an extrinsic basis. *Computer Modeling in Engineering and Sciences* 2006; **16**(2):115–130.
29. Donning BM, Liu WK. Meshless methods for shear-deformable beams and plates. *Computer Methods in Applied Mechanics and Engineering* 1998; **152**(1–2):47–71.
30. Liu WK, Jun S, Zhang YF. Reproducing kernel particle methods. *International Journal for Numerical Methods in Fluids* 1995; **20**(8–9):1081–1106.
31. Liu WK, Jun S, Li SF, Adee J, Belytschko T. Reproducing kernel particle methods for structural dynamics. *International Journal for Numerical Methods in Engineering* 1995; **38**(10):1655–1679.
32. Kanok-Nukulchai W, Barry W, Saran-Yasoontorn K, Bouillard PH. On elimination of shear locking in the element-free Galerkin method. *International Journal for Numerical Methods in Engineering* 2001; **52**(7):705–725.
33. Noguchi H, Kawashima T, Miyamura T. Element free analyses of shell and spatial structures. *International Journal for Numerical Methods in Engineering* 2000; **47**(6):1215–1240.
34. Garcia O, Fancello EA, de Barcellos CS, Duarte CA. *hp*-Clouds in Mindlin's thick plate model. *International Journal for Numerical Methods in Engineering* 2000; **47**(8):1381–1400.
35. Leitao VMA. A meshless method for Kirchhoff plate bending problems. *International Journal for Numerical Methods in Engineering* 2001; **52**(10):1107–1130.
36. Liew KM, Chen XL. Mesh-free radial point interpolation method for the buckling analysis of Mindlin plates subjected to in-plane point loads. *International Journal for Numerical Methods in Engineering* 2004; **60**(11): 1861–1877.
37. Liew KM, Chen XL. Buckling of rectangular Mindlin plates subjected to partial in-plane edge loads using the radial point interpolation method. *International Journal of Solids and Structures* 2004; **41**(5–6):1677–1695.
38. Atluri SN, Cho JY, Kim HG. Analysis of thin beams, using the meshless local Petrov–Galerkin method, with generalized moving least squares interpolations. *Computational Mechanics* 1999; **24**(5):334–347.
39. Long SY, Atluri SN. A meshless local Petrov–Galerkin method for solving the bending problem of a thin plate. *Computer Modeling in Engineering and Sciences* 2002; **3**(1):53–63.
40. Soric J, Li Q, Jarak T, Atluri SN. Meshless local Petrov–Galerkin (MLPG) formulation for analysis of thick plates. *Computer Modeling in Engineering and Sciences* 2004; **6**(4):349–357.
41. Sladek J, Sladek V, Wen PH, Aliabadi MH. Meshless local Petrov–Galerkin (MLPG) method for shear deformable shells analysis. *Computer Modeling in Engineering and Sciences* 2006; **13**(2):103–117.
42. Jarak T, Soric J, Hoster J. Analysis of shell deformation responses by the meshless local Petrov–Galerkin (MLPG) approach. *Computer Modeling in Engineering and Sciences* 2007; **18**(3):235–246.
43. Li Q, Soric J, Jarak T, Atluri SN. A locking-free meshless local Petrov–Galerkin formulation for thick and thin plates. *Journal of Computational Physics* 2005; **208**(1):116–133.
44. Chen JS, Wang DD. A constrained reproducing kernel particle formulation for shear deformable shell in Cartesian coordinates. *International Journal for Numerical Methods in Engineering* 2006; **68**(2):151–172.
45. Wang DD, Chen JS. A locking-free meshfree curved beam formulation with the stabilized conforming nodal integration. *Computational Mechanics* 2006; **39**(1):83–90.
46. Yagawa G, Miyamura T. Three-node triangular shell element using mixed formulation and its implementation by free mesh method. *Computers and Structures* 2005; **83**(25–26):2066–2076.
47. Li S, Hao W, Liu WK. Numerical simulations of large deformation of thin shell structures using meshfree methods. *Computational Mechanics* 2000; **25**(2–3):102–116.
48. Lu HS, Cheng HS, Cao J, Liu WK. Adaptive enrichment meshfree simulation and experiment on buckling and post-buckling analysis in sheet metal forming. *Computer Methods in Applied Mechanics and Engineering* 2005; **194**(21–24):2569–2590.

DOI: 10.1002/nme

49. Zhou M, Ravichandran G, Rosakis AJ. Dynamically propagating shear bands in impact-loaded prenotched plates. 2. Numerical simulations. *Journal of the Mechanics and Physics of Solids* 1996; **44**(6):1007–1032.
50. Li SF, Liu WK, Qian D, Guduru PR, Rosakis AJ. Dynamic shear band propagation and micro-structure of adiabatic shear band. *Computer Methods in Applied Mechanics and Engineering* 2001; **191**(1–2):73–92.
51. Taylor GI, Quinney H. The latent energy remaining in a metal: after cold working. *Proceedings of the Royal Society of London*, *Series A* 1934; **143**:307–326.
52. Li SF, Liu WK. Numerical simulations of strain localization in inelastic solids using mesh-free methods. *International Journal for Numerical Methods in Engineering* 2000; **48**(9):1285–1309.
53. Ji Z, Deng KS, Davies AW, Williams FW. Numerical modelling of thermal destruction of cylindrical shells with internal pre-pressure under laser irradiation. *Computers and Structures* 1999; **71**(4):359–370.
54. Peirce D, Shih CF, Needleman A. A tangent modulus method for rate dependent solids. *Computers and Structures* 1984; **18**(5):875–887.
55. Armero F, Simo JC. A new unconditionally stable fractional step method for nonlinear coupled thermomechanical problems. *International Journal for Numerical Methods in Engineering* 1992; **35**(4):737–766.
56. Liu WK, Belytschko T. Mixed-time implicit-explicit finite-elements for transient analysis. *Computers and Structures* 1982; **15**(4):445–450.
57. Belytschko T, Smolinski P, Liu WK. Stability of multi-time step partitioned integrators for 1st-order finite-element systems. *Computer Methods in Applied Mechanics and Engineering* 1985; **49**(3):281–297.
58. Krysl P, Belytschko T. Element-free Galerkin method: convergence of the continuous and discontinuous shape functions. *Computer Methods in Applied Mechanics and Engineering* 1997; **148**(3–4):257–277.

DOI: 10.1002/nme